厚生労働科学研究費補助金
医療機器開発推進研究事業

循環器病治療機器の医工連携による研究開発・製品化・汎用化を実現するための基盤整備に関する研究（H20-医工-一般-002）

平成２１年度　総括・分担研究報告書

研究代表者　妙中　義之

平成２２（２０１０）年４月

２／３冊

Artificial Organs
33(12):1127–1135, Wiley Periodicals, Inc.

Thoughts and Progress

An Animal Study of a Newly Developed Skin-Penetrating Pad and Covering Material for Catheters to Prevent Exit-Site Infection in Continuous Ambulatory Peritoneal Dialysis

*†Masato Aoyama, †Toshihide Mizuno, †Eisuke Tatsumi, †Yoshiyuki Taenaka, ‡Yasushi Nemoto, ‡Yoshihiro Okamoto, *Yoshiaki Takemoto, *Toshihide Naganuma, and *Tatsuya Nakatani*

**Department of Urology, Osaka City University Medical School, Osaka; †Department of Artificial Organs, Research Institute, National Cardiovascular Center, Suita; and ‡Development Department, Chemical Products Division, Bridgestone Corporation, Yokohama, Kanagawa, Japan*

Abstract: Because currently available peritoneal dialysis catheters are not sufficiently biocompatible with the skin and subcutaneous tissue at the site of penetration, exit-site infection due to pericatheter pocket formation caused by epidermal downgrowth over a long period of time has increasingly become a problem. We developed a new, biocompatible, segmented polyurethane porous material and devised a novel skin-penetrating pad, the form and material of which we optimized for application in peritoneal dialysis catheters. For the extent of tissue ingrowth into this porous material to be examined, test materials with different pore diameters were inserted into hollow silicone tubes and implanted in the subcutaneous tissue of a goat. Four weeks later, the tubes were extracted, and, after the extent of granulation tissue ingrowth was measured, histopathological evaluation was made. Our novel skin-penetrating pad has three disklike layers of the segmented polyurethane material with different pore sizes, into the center of which a polyurethane catheter is inserted. These pads were implanted in the skin of a goat and clinically observed over a 2-year period, after which they were extracted and histopathologically analyzed. In accordance with actual clinical procedures, a commercial CAPD catheter equipped with our skin-penetrating pad was left indwelling in a goat for 4 months, and the performance of the pad was evaluated after repeated periodic infusion and drainage of the dialysate in and out of the abdominal cavity. There was no inflammation of the ingrown tissue in the pores of the segmented polyurethane material as well as the surrounding tissue, which indicated favorable tissue biocompatibility. The extent of tissue ingrowth was greater as the pore size of the material was larger, and the tissue tended to be mature, mainly consisting of collagenous fibers. The skin-penetrating pad using the porous material, of which tissue ingrowth was thus optimized, tightly adhered to the goat skin throughout the 2-year experimental period without any special wound care such as cleansing or disinfection. The performance of the skin-penetrating pad was similarly favorable when attached to a commercial continuous ambulatory peritoneal dialysis catheter. The newly developed segmented polyurethane porous material had excellent tissue biocompatibility and tissue ingrowth. The skin-penetrating pad devised by using this porous material did not cause epidermal downgrowth, suggesting that it may be effective for the prevention of exit-site infection. **Key Words:** Skin-penetrating pad—Continuous ambulatory peritoneal dialysis—Exit-site infection.

In continuous ambulatory peritoneal dialysis (CAPD), which is an effective therapeutic procedure for chronic renal failure and end-stage renal disease, the prevention of catheter exit-site infection is one of the most important challenges in conducting long-term treatment safely (1). The main source of this infection is the dead space that is formed by epidermal invagination along the catheter (epidermal downgrowth) at the site of skin penetration (2), and bacterial proliferation and bleeding in these pockets are considered to exacerbate infection during CAPD (3). For this exit-site infection to be prevented, the periodic topical application of antibiotics on the skin is considered effective, but, despite increasing treatment periods, measures against drug-resistant bacteria have yet to be established (4,5). Moreover, for the CAPD catheter to be firmly attached to the surrounding living tissue, devices such as an alumina ceramic percutaneous terminal, titanium fiber mesh skin-penetrating device, expanded polytetrafluoroethylene skin-penetrating device, and solid polyurethane catheter covering material have been developed, and attempts have been made to apply them to catheters, but none have been put to practical use (6–9).

In this study, in order to prevent exit-site infection, we developed a segmented polyurethane porous material that is flexible and biocompatible and can be subjected to long-term indwelling, and

doi:10.1111/j.1525-1594.2009.00805.x

Received March 2008; revised October 2008.
Address correspondence and reprint requests to Dr. Masato Aoyama, Department of Urology, Osaka City University Medical School, 4-3 Asahimachi 1-chome, Abeno-ku, Osaka, 545-8585, Japan. E-mail: masatoaym@msic.med.osaka-cu.ac.jp

investigated its optimal properties, pore size, and tissue ingrowth so that the catheter can tightly adhere to the surrounding tissue during actual use. Furthermore, we created a novel skin-penetrating pad by devising a unique form to prevent epidermal downgrowth and to inhibit damage of the surrounding tissue by external pressure to the catheter and optimized its form and material for application in CAPD catheters.

MATERIALS AND METHODS

Development of a new, segmented polyurethane porous material

We newly developed a segmented polyurethane porous material using Miractran (E980, Nippon Miractran, Kanagawa, Japan), a polycarbonate segmented polyurethane resin. This material, whose pore diameter can be freely adjusted within the range of approximately 100–1000 μm, had a three-dimensional reticulated microstructure consisting of a relatively thick framework, with many micropores of approximately 10–50 μm in pore diameter within the framework (Fig. 1). This porous material does not produce a dense surface layer due to a new manufacturing process and can be formed into various shapes with a curved surface, as the removal of dense layers by slicing is not necessary (Fig. 2). In this study, we prepared test materials with different pore sizes and evaluated the changes in their properties. For the measurement of pore size and its distribution, images were taken and examined by using a scanning electron microscope (SM200, Topcon Technohouse Corporation, Tokyo, Japan)

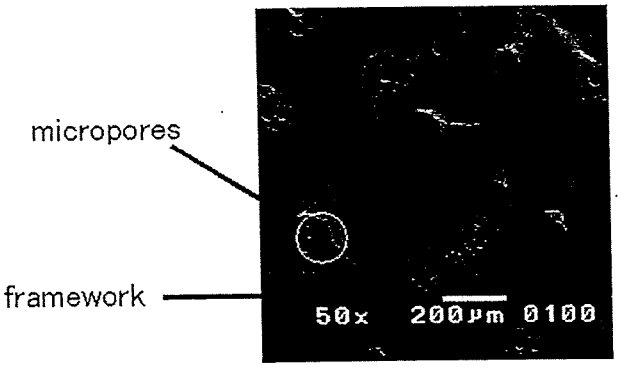

FIG. 1. Scanning electronmicrograph photograph of the new porous material. The segmented polyurethane porous material has a three-dimensional reticulated microstructure consisting of a relatively thick framework with many micropores of approximately 10–50 mm in pore diameter within the framework.

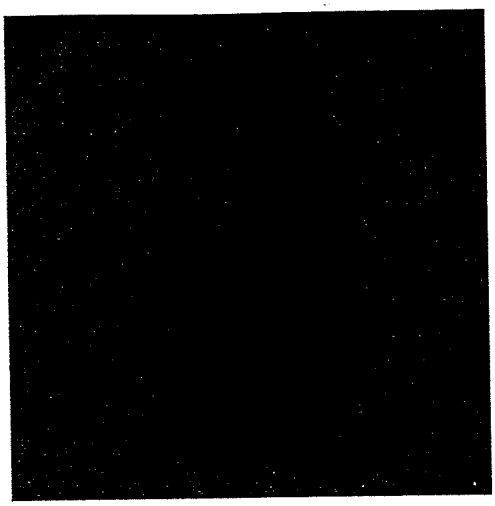

FIG. 2. Photograph of the tube-shaped porous material. Our material can be formed into complicated shapes while maintaining its continuous porous microstructure.

and a microscope (VH-6300, Keyence Corporation, Osaka, Japan). The pores on the same surface of the images were manually extracted and uploaded again onto our computer, and the pore size and its distribution were measured by using an image processing system (LUZEX AP, Nireco Corporation, Tokyo, Japan). Test materials with mean pore diameters of 490, 290, and 41 μm were prepared ($n = 3$), and the tensile testing was conducted at load cell of 50 N, dumbbell-shape DIM 3 type, tensile rate of 100 mm/min, gauge length of 10 mm, and chuck distance of 30 mm by using a precision universal tensile testing machine (Autograph AG-1, Shimadzu, Kyoto, Japan).

Biocompatibility of the newly developed porous material

For the changes in the extent of tissue ingrowth according to the pore size of this material to be studied, cylindrically shaped test materials with pore diameters of 500, 300, 150, and 50 μm inserted in open-ended silicone tubes (length: 3 cm, inner diameter: 3 mm, $n = 5$) were prepared (Fig. 3). These test materials were surgically implanted in the subcutaneous tissue on the back of an adult female goat weighing 60 kg under general anesthesia with isoflurane. Four weeks later, the goat was euthanized, and the test materials were extracted along with the surrounding tissue and fixed in 10% neutral buffered formalin. The extracted materials were sliced longitudinally to prepare thin sections, which were examined by using a light microscope after Azan staining. The extent of granulation tissue ingrowth in the tube

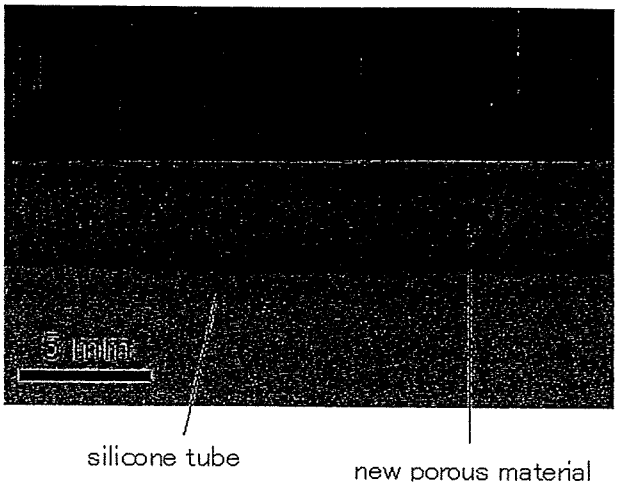

FIG. 3. Photograph of the test material.

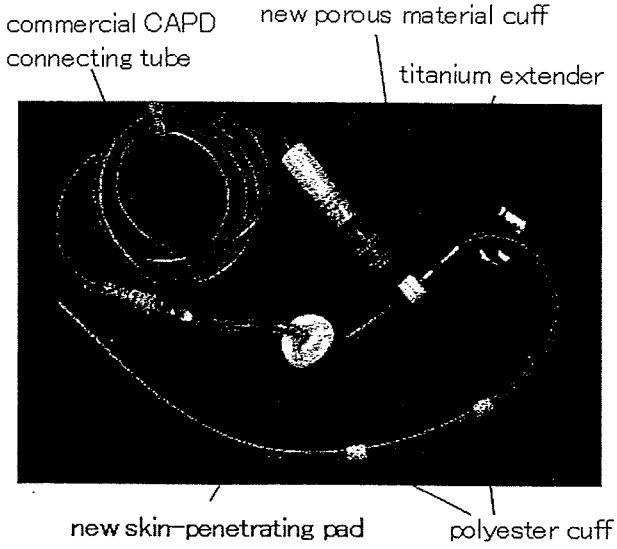

FIG. 5. Photograph of the skin-penetrating pad and porous material cuff connected to a CAPD catheter by using a titanium extender.

from the open end was measured, and its histopathological findings were investigated.

Development of a novel CAPD catheter skin-penetrating pad and cuff using the newly developed porous material

Our novel skin-penetrating pad has three disklike layers of the segmented polyurethane material, which is surgically implanted at the site of catheter penetration. The lowest flange-shaped layer of this pad consisting of large pore size material due to its favorable tissue ingrowth was designed to adhere to the subcutaneous tissue without inhibiting blood flow to the epidermis. The middle layer consisting of slightly smaller pore size material was intended to adhere to the epidermis and prevent downgrowth. The topmost layer made of nonporous material was designed to separate the catheter, which is subject to contamination, from the outer edge of the flange part that adheres to the skin as well as protect the wound by absorbing the external pressure to the catheter (Fig. 4). Thanks to this structure, this device was thought to very firmly adhere to the skin, highly preventing infection. In order to study the biocompatibility of this pad and its effects on exit-site infection, we created prototypes of the skin-penetrating pad and surgically implanted them on the back skin of an adult goat that was kept under observation over a 2-year period. No wound care such as disinfection and draping was conducted except for the acute phase immediately after surgery. In addition, the skin-penetrating pad and porous material cuff were connected to a commercial CAPD catheter by using a titanium extender (Fig. 5), which was surgically placed long term into the abdominal cavity and subcutaneously tunneled and exteriorized. The goat

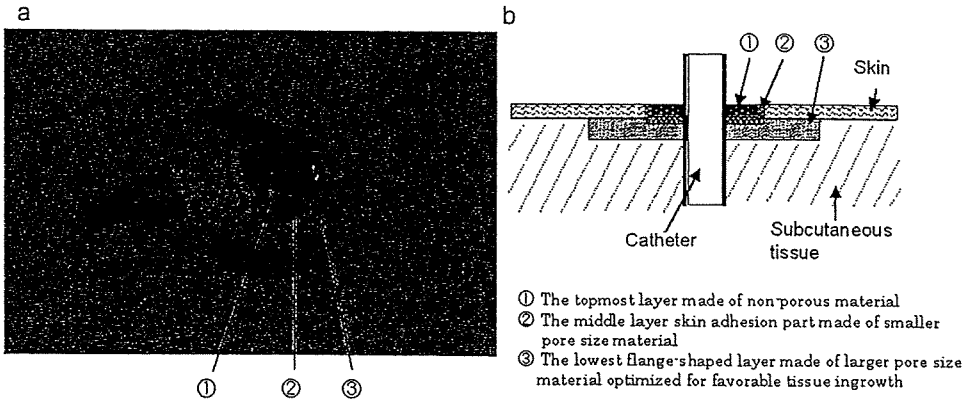

FIG. 4. (a) Photograph of the new skin-penetrating pad. (b) Illustration of the new skin-penetrating pad implanted in the skin.

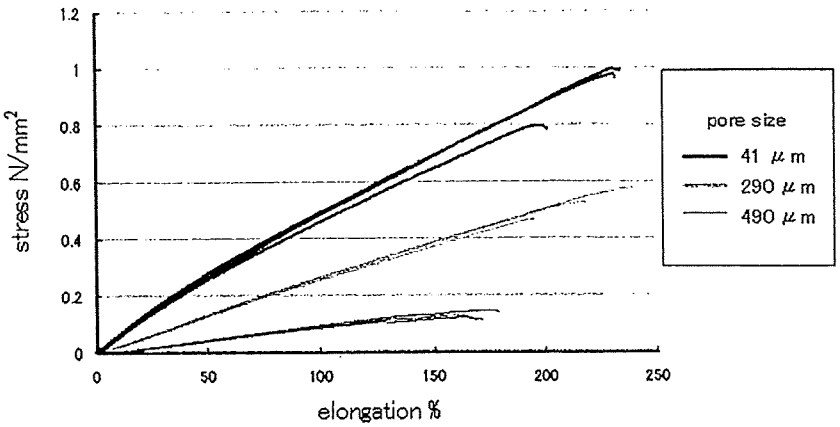

FIG. 6. Stress–strain curves of our porous materials.

actually underwent peritoneal dialysis (once a week, 2000 mL peritoneal dialysate) and was kept under observation for 120 days. After both experiments, the catheter was extracted, and pathological analysis was carried out. As the control, a polyester cuff was used, and the difference with our porous material was also studied. These experiments were conducted based on the Animal Experiment Guidelines of the National Cardiovascular Center under the approval of its Animal Experiment Committee.

RESULTS

Development of a new, segmented polyurethane porous material

The results of the tensile test showed that, upon rupture, the test material with an average pore diameter of 490 μm had a mean stress of 0.13 N/mm² and a mean elongation rate of 167% (δ6.93%); that, with an average pore diameter of 290 μm, had a mean stress of 0.52 N/mm² and mean elongation rate of 215% (δ22.03%); and that, with an average pore diameter of 41 μm, had a mean stress of 0.92 N/mm² and mean elongation rate of 219% (δ19.05%) (Fig. 6).

Biocompatibility of the newly developed porous material

Histological examination of the test tubes implanted to evaluate the extent of tissue ingrowth after 1 month showed granulation tissue ingrowth from both ends of the cylindrically shaped porous material, making separation of the material and living tissue extremely difficult. The length of granulation tissue ingrowth in the test tube was 4.0 ± 0.7, 5.4 ± 0.9, 6.6 ± 0.6, and 7.2 ± 1.2 cm for the test materials with average pore diameters of 50, 150, 300, and 500 μm, respectively ($n = 5$), and, for the materials with pore diameters of 50–300 μm, the larger the pore size, the greater was the extent of tissue ingrowth. For the materials with pore diameters of 300 μm and more, the length of tissue ingrowth formed a plateau at approximately 7.0 cm (Fig. 7). Histopathologically, the materials with large pore diameters (300–500 μm) had favorable mature adhesive tissue ingrowth mainly consisting of collagenous fibrous tissue, and tissue vascularization at the same site was also frequently observed. In addition, there was no infection or necrosis of the ingrown tissue in all of the groups.

Development of a CAPD catheter skin-penetrating pad and cuff using the newly developed porous material

Throughout the 2-year experimental period, there was no indication of infection such as reddening, swelling, or purulent discharge of the skin around the device or any spontaneous desquamation as a reaction to rejection of foreign material, and the pads tightly adhered to the skin. Every day, the catheter

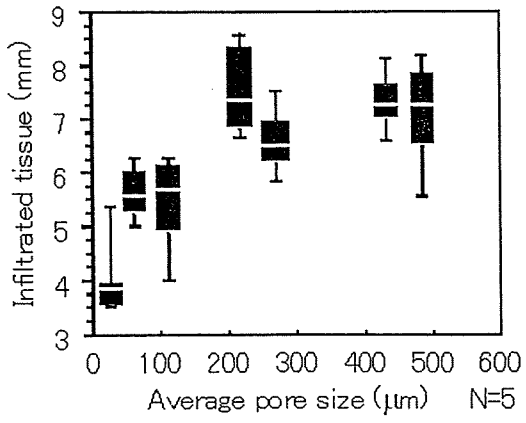

FIG. 7. The extent of tissue ingrowth increased in proportion to material pore size.

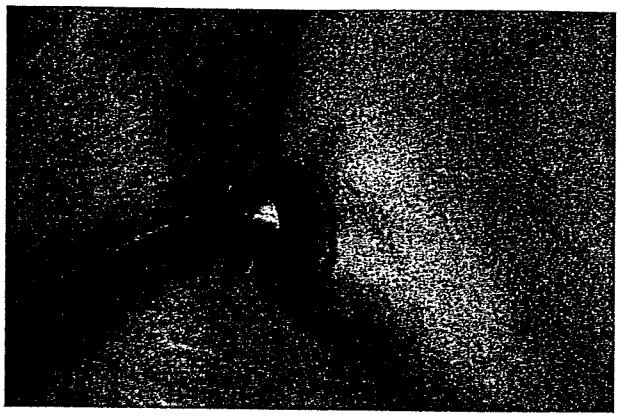

FIG. 8. Photograph of the implanted skin-penetrating pad. There was no infection or rejection of foreign material, and the pads tightly adhered to the skin. There was also no damage to the pad itself.

part was strongly pulled in various directions, but there was no subcutaneous disturbance of the flange part or damage to the pad itself (Fig. 8). When the extracted specimen was observed from the side of the subcutaneous tissue, the flange part was abundantly covered with vascularized tissue. There were no other findings such as abscesses under the skin. When the specimen was sliced along the catheter, no pocket formation due to epidermal downgrowth at the outer edge of the topmost layer was seen. The lowest layer was integrated with the surrounding tissue by abundant tissue ingrowth and could not be separated (Fig. 9). In the dialysis experiment using the CAPD catheter equipped with the skin-penetrating pad and cuff, the dialysate could be infused and drained without problem, and there was no damage such as detachment of the device from the skin despite considerable external pressure load to the catheter during infusion and drainage. Histological analysis showed that the ingrown granulation tissue between the fibers of the polyester cuff was mainly immature granulation tissue mostly consisting of fibroblastic cells, but the ingrown granulation tissue in the porous material cuff was mainly mature collagenous fibrous tissue (Fig. 10).

DISCUSSION

As our basic approach toward the development of the new skin-penetrating pad, the following three points were taken into consideration: (i) selecting a polymeric material that has favorable biocompatibility and superior long-term mechanical and chemical durability; (ii) developing a material that has a continuous porous microstructure that can tightly adhere to the subcutaneous tissue; and (iii) designing a macrostructure that can disperse the repeated external pressure from the catheter and prevent epidermal downgrowth.

We selected Miractran, which is a polycarbonate segmented polyurethane resin, as the polymeric material. This material is used in undulating artificial heart diaphragms and has superior mechanical durability and flexibility. As it is also hypoallergenic, we decided that it was appropriate to use as the material for our skin-penetrating pad. From this, we succeeded in producing a new porous material that fitted our purposes using a newly developed manufacturing process (patent pending), enabling the pore diameter and pore rate to be adjusted. As for the macrostructure, we devised a three-layer structure, with each layer consisting of the material featuring different characteristics, efficiently dispersing the external pressure from the catheter and preventing epidermal downgrowth.

The newly developed porous material firmly adhered to the surrounding tissue when implanted and maintained flexibility with little burden on the surrounding tissue as well as having enough strength against external force, even though it had a pore size

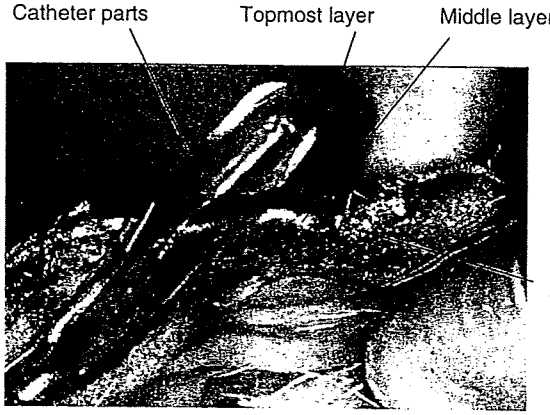

FIG. 9. Photograph of the specimen sliced along the catheter. No pocket formation due to epidermal downgrowth at the outer edge of the topmost layer was seen. The lowest layer was integrated with the surrounding tissue by abundant tissue ingrowth and could not be separated.

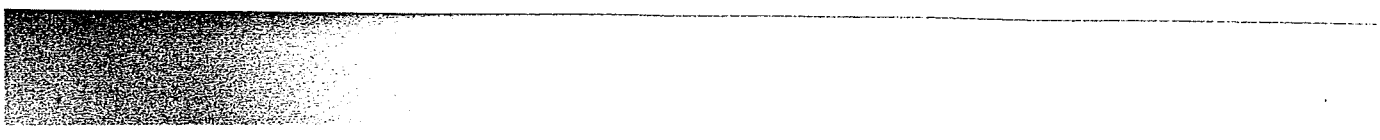

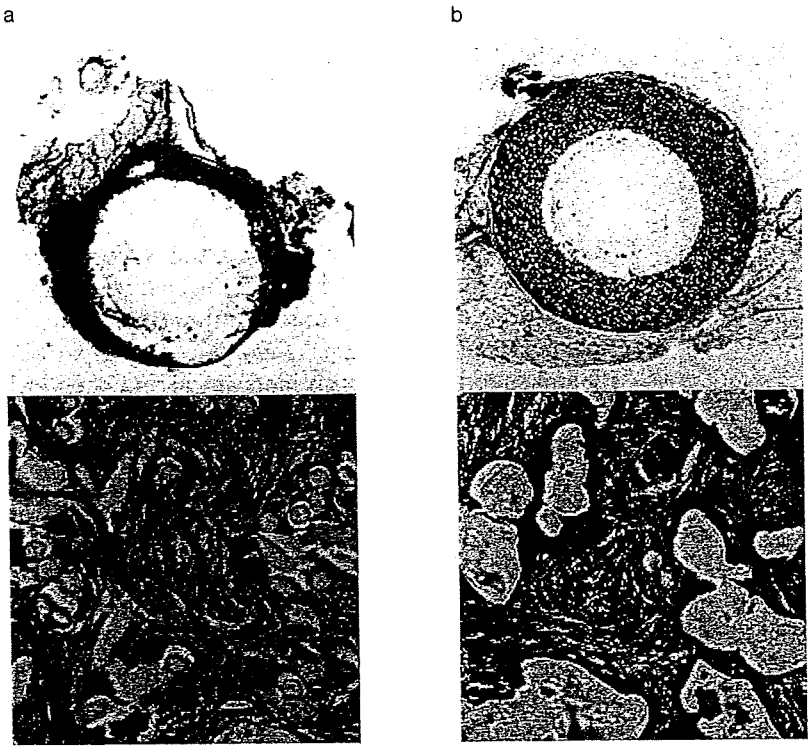

FIG. 10. Histological analysis showed that the ingrown granulation tissue between the fibers of the polyester cuff was mainly immature granulation tissue mostly consisting of fibroblastic cells (a), but the ingrown granulation tissue in the porous material cuff was mainly mature collagenous fibrous tissue (b).

that enabled sufficient ingrowth of granulation tissue and vascularization. The granulation tissue that infiltrated the porous material was mature and abundant in collagenous fibers compared with the polyester nonwoven material, which also indicated that it was effective in maintaining long-term adhesion. Furthermore, the novel skin-penetrating pad did not require any wound care including disinfection during the 2-year experimental period, and there was no indication of exit-site infection such as necrosis of the surrounding tissue or other infection during the experiment as well as at autopsy, demonstrating that it was effective for the inhibition of epidermal downgrowth.

The predicted advantages of the clinical application of this novel skin-penetrating pad are as follows: (i) the improvement of patient quality of life because the patient is liberated from exit-site care; (ii) decrease in the amount of disinfectants, film dressing materials, and antibiotics needed for catheter care; and (iii) decrease in treatment frequency of catheter problems such as exit-site infection with an accompanying reduction in medical cost. As a disadvantage, the skin and subcutaneous tissue must be removed when the skin-penetrating pad is removed with the catheter, but this is believed to be well within the range of tolerance, considering its major merits such as simplified management and suppression of infections.

CONCLUSION

The newly developed segmented polyurethane porous material had excellent strength, flexibility, durability, biocompatibility, and tissue ingrowth. The novel skin-penetrating pad, which was devised by using this material, firmly adhered to the tissue and did not cause epidermal downgrowth at the site of catheter penetration, which suggested that it may be effective in preventing exit-site infection.

REFERENCES

1. Twardowski ZJ. Peritoneal access: the past, present, and the future. *Contrib Nephrol* 2006;150:195–201.
2. Knabe C, Grosse-Siestrup C, Gross U. Histologic evaluation of a natural permanent percutaneous structure and clinical percutaneous devices. *Biomaterials* 1999;20:503–10.
3. Gokoo CF, Lelah MD, Hauck W, Burhop KE. External catheter immobilization improves wound healing in micropigs. *ASAIO Trans* 1989;35:412–4.
4. Thodis E, Bhaskaran S, Pasadakis P, Bargman JM, Vas SI, Oreopoulos DG. Decrease in staphylococcus aureus exit-site infections and peritonitis in CAPD patients by local application of mupirocin ointment at the catheter exit site. *Perit Dial Int* 1998;18:261–70.
5. Annigeri R, Conly J, Vas S, et al. Emergence of mupirocin-resistant staphylococcus aureus in chronic peritoneal dialysis

patients using mupirocin prophylaxis to prevent exit-site infection. *Perit Dial Int* 2001;21:554–9.
6. Amano I, Katoh T, Inagaki Y. Development of alumina ceramic transcutaneous connector to prevent skin exit site infections around CAPD catheters. *ASAIO Trans* 1990;36:M494–6.
7. Paquay YC, de Ruijter JE, van der Waerden JP, Jansen JA. Tissue reaction to Dacron velour and titanium fibre mesh used for anchorage of percutaneous devices. *Biomaterials* 1996; 17:1251–6.
8. Bay WH, Vaccaro PS, Powell SL, Erlich LF. The Gore-Tex peritoneal catheter: a clinical evaluation and comparison with the Tenckhoff catheter. *Am J Kidney Dis* 1984;4:268–79.
9. Daly BD, Dasse KA, Gould KE, et al. A new percutaneous access device for peritoneal dialysis. *ASAIO Trans* 1987;33: 664–71.

Forward Osmosis Process for Dialysis Fluid Regeneration

Khaled Mohamed Talaat
Department of Internal Medicine, Faculty of Medicine, Zagazig University, Zagazig, Egypt

Abstract: In a preliminary experiment, 38% of the spent dialysis fluid water was reclaimed by a forward osmosis process through a cellulose triacetate membrane. The simplicity of forward osmosis and its minimal external energy requirements may allow the construction of a small bulk device that can reclaim a considerable portion of the water used in the patient's dialysis process. For developing an acceptable ambulatory dialysis system, decreasing the bulk of the fluid and equipment carried on the patient is essential. Forward osmosis may feasibly be used for dialysis fluid regeneration in ambulatory dialysis systems. **Key Words:** Ambulatory—Dialysis—Dialysis solution regeneration—Osmosis—Forward osmosis.

In the forward osmosis process, water is drawn across a water-permeable but solute-impermeable membrane from the feed solution into the more concentrated draw solution down the concentration gradient (1). The cellulose triacetate (CTA) membrane was made by Hydration Technologies, Inc. (Albany, OR, USA). The CTA membrane has outperformed other membranes in forward osmosis applications. The structure and the performance of this membrane have been reviewed (2–3). An example of the current applications of forward osmosis is the hydration bags made by Hydration Technologies, Inc. Hydration bags consist of an external feed solution compartment that is filled with either sea water or unsafe water, and an internal draw solution compartment made of the CTA membrane. Water is drawn from the feed solution through the CTA membrane to dilute a concentrated sugary draw solution generating a safe-to-drink sugary beverage. In the current investigation, the potential use of the forward osmosis process for dialysis fluid regeneration was examined. A concentrated sodium chloride solution was used to draw water from the spent dialysis fluid across the same CTA membrane.

MATERIALS AND METHODS

In the current investigation, a sample of the spent dialysis fluid was collected 15 min after starting the patient's dialysis session. Before starting the forward osmosis experiment, the CTA membrane of the osmosis bag (the SeaPack made by Hydration Technologies, Inc.) was prehydrated by washing the two compartments of the osmosis bag with 0.45% saline. The saline was then drained before introducing 250 mL of the spent dialysis fluid into the feed solution compartment and 20 mL of 10% sodium chloride (Na^+ concentration = 1711 mmol/L) into the draw solution compartment. The forward osmosis process was carried out for 3 h at 35°C, while the osmosis bag was shaken on an automatic shaker that delivered 10-cm horizontal displacement at a frequency of 60 cycles/min. These experimental settings were found to increase the water reclamation rate in the initial trials. The feed and the draw solution were drained hourly. Their volume and sodium concentration were then determined before reintroducing them into the forward osmosis bag. Creatinine, urea, uric acid, phosphate, sodium, potassium, calcium, and magnesium were measured in the feed solution at the start of both experiments and in the draw solution at the end of the experiment. Water reclamation ratio was calculated as the gain in the draw solution volume / 250 × 100%. Sodium back-leak into the feed solution was calculated as the decrease in the Na^+ content of the draw solution / its initial Na^+ content at the start of the experiment × 100%. In the initial stages of the experiment, a search for the best settings that gave the highest water reclamation rate was done. The previously described shaking, membrane prehydration, and temperature gave the optimal results. The best obtained results were represented.

RESULTS

At the start of the experiment, the concentration of urea in the spent dialysis fluid solution was 32 mmol/L, creatinine 796 μmol/L, uric acid 635 μmol/L, calcium 1.1 mmol/L, magnesium

doi:10.1111/j.1525-1594.2009.00816.x

Received June 2008; revised October 2008.

Address correspondence and reprint requests to Professor Khaled Mohamed Talaat, Department of Internal Medicine, Faculty of Medicine, Zagazig University, Zagazig, PO 44519, Egypt. E-mail: k_m_talaat@yahoo.com

TABLE 1. *Volume, Na^+ concentration, water reclamation, and Na^+ back-leak*

	At start	1 h	2 h	3 h
Draw solution volume (mL)	20	62	90	114
Feed solution volume (mL)	250	208	180	156
Draw solution Na^+ (mmol/L)	1711	550	378	289
Feed solution Na^+ (mmol/L)	138	166	193	223
Water reclamation (%)	0	17	28	38
Sodium back-leak (%)	0	0.3	0.5	0.7

1.4 mmol/L, potassium 4.9 mmol/L, and phosphorus 1.6 mmol/L. Creatinine, uric acid, potassium, calcium, magnesium, and phosphorus were undetectable in the draw solution at the end of the experiment. In contrast, the draw solution urea concentration was 12 mmol/L at the end of the experiment. The hourly volume of the draw and the feed solutions, their sodium concentration, as well as the water reclamation ratio and the sodium back-leak, are shown in Table 1.

DISCUSSION

After 3 h of forward osmosis, 38% of the water content of the spent dialysis fluid was reclaimed and 114 mL of fluid was obtained from the draw solution compartment of the osmosis bag. The draw solution sodium concentration at the end of experiment dropped to 298 mmol/L. If the obtained fluid is used for fresh dialysis fluid preparation, dilution with 129 mL of exogenous free water is necessary to bring its sodium concentration down to 140 mmol/L, which is the usual concentration used in clinical dialysis. The CTA membrane completely rejected potassium, calcium, magnesium, and phosphate, which are highly charged ions. Similarly, the rejection of the two tested weakly charged substances with high molecular weight was complete. Creatinine, whose molecular weight (MW) = 113, and uric acid (MW = 168), were completely rejected while the rejection of the uncharged small urea molecule (MW = 60) was much less. The purpose of the use of forward osmosis in dialysis fluid regeneration is to build a small ambulatory dialysis system that can conveniently be used for extended time dialysis prescription, for example, 10–12 h of dialysis therapy/day. The basic requirements of the system are simple: a low pressure pump and the forward osmosis membrane. Minimal external energy supply is needed because the concentration difference between the feed and the draw solution is the source of the thermodynamic energy that drives the process. Moreover, the required volume of the exogenous solutions is reduced because a substantial portion of the dialysis fluid water is recycled. Consequently, extended time ambulatory dialysis with dialysis fluid regeneration may be an acceptable option that may offer definite therapeutic advantages. First, a much higher clearance of middle- and high-molecular-weight uremic toxins may be achieved by an extended time dialysis prescription utilizing a highly permeable hemodialyzer optimized for the removal of those molecules. Also, an accompanying slow extended time ultrafiltration has important cardiovascular advantages. In the current experiment, two drawbacks of the proposed concept were found. First, the obtained fluid on the draw solution side of the membrane will always be hyperosmolar compared to the spent dialysis fluid. Consequently, dilution with free water is necessary. Possible sources of the required free water include:

1. Free water carried in a refillable reservoir attached to the system.
2. The permeate resulting from a reverse osmosis treatment.
3. Oral water intake by the patient during the prolonged ambulatory dialysis session combined with ultrafiltration. Deliberate slight dialysis fluid hypernatremia may create a robust physiological drive for increased water intake while the resultant hypervolemia is corrected by ultrafiltration.
4. A combination of the previously mentioned methods.

The second drawback is the suboptimal urea rejection ratio. Urea has no or minimal clinical toxicity (4). Consequently, the observed low urea rejection ratio is not likely to compromise the clinical outcome when forward osmosis is used for dialysis fluid regeneration. However, a dual modality therapy consisting of a short home hemodialysis treatment for 1–2 h/day and an extended ambulatory treatment with dialysis fluid regeneration may not greatly compromise the patient's lifestyle. The dual modality therapy may also provide the opportunity to target the small and the larger uremic toxins with two hemodialysis membranes, each optimized for the removal of solutes with a particular range of molecular sizes.

CONCLUSION

Forward osmosis process is a feasible and simple method that may be suitable for use in dialysis fluid regeneration systems. However, it is necessary to construct a forward osmosis device that is specifically devoted for dialysis fluid regeneration and test its performance in water retrieval and uremic solute rejection in vitro before conducting animal studies.

REFERENCES

1. Cath TY, Childress AE, Elimelech M. Forward osmosis: principles, applications, and recent developments. *J Membr Sci* 2006;28:70–87.
2. Cath TY, Gormly S, Beaudry EG, Flynn MT, Adams VD, Childress AE. Membrane contactor processes for wastewater reclamation in space: Part I. Direct osmosis concentration as pretreatment for reverse osmosis. *J Membr Sci* 2005;257:85–98.
3. McCutcheon JR, McGinnis RL, Elimelech M. Desalination by ammonia–carbon dioxide forward osmosis: influence of draw and feed solution concentration on process performance. *J Membr Sci* 2006;278:114–23.
4. Johnson WJ, Hagge WW, Wagoner RD, Dinapoli RP, Rosevear JW. Effects of urea loading in patients with far-advanced renal failure. *Mayo Clin Proc* 1972;47:21–9.

J Artif Organs (2009) 12:105–110
DOI 10.1007/s10047-009-0458-3

ORIGINAL ARTICLE

Hwansung Lee, PhD · Akihiko Homma, PhD
Eisuke Tatsumi, MD, PhD
Yoshiyuki Taenaka, MD, PhD

Observation of cavitation pits on a mechanical heart valve surface in an artificial heart used in in vivo testing

Abstract The aim of this study was to observe mechanical heart valve (MHV) cavitation pits resulting from in vivo testing of an electrohydraulic total artificial heart (EHTAH). During in vivo testing with three sets of valves (one set used in two animals), the slope of the driving pressure (left and right driving pressure) was used as a factor for investigating cavitation intensity, and the occurrence of cavitation was determined by the observation of cavitation pits on the explanted valve surfaces. Medtronic Hall valves were installed at the inlet and outlet positions of the two blood pumps. The EHTAH was tested using calves weighing 69–80 kg. The cavitation pits on the valve surface of the inlet valves of the left and right blood pumps were examined by scanning electron micrography. The driving pressure slope 5 ms before valve closure exceeded the cavitation threshold during in vitro testing. On both inlet valves, many large pits formed when the driving pressure slope was high and the pump operating time was long. When estimating cavitation intensity during in vivo testing, both a high driving pressure slope and a long operating time are important factors. The cavitation pits observed on the valve surfaces resulting from in vivo testing will eventually lead to leaflet fracture.

Key words Electrohydraulic total artificial heart · Mechanical heart valve · Cavitation · Cavitation pits

Introduction

Cavitation is the rapid formation and collapse of vapor-filled cavities when a liquid is exposed to rapid changes in pressure below its vapor pressure.[1,2] When cavitation occurs near the material surface of a mechanical heart valve, this rapid collapse may cause a high-speed microjet and shock waves, which cause cavitation erosion on the valve surface[3–5] and may be a source of blood damage.[6,7] Commercial mechanical heart valves were developed not for use in artificial hearts, but rather for use as valve replacements in the clinical setting. In general, the mechanical heart valves used here were rigidly mounted in an artificial heart after the sewing rings had been removed, resulting in much faster valve closure and stronger cavitation intensity than that found in the context of valve replacements in the clinical setting. Pyrolytic carbon has good biocompatibility and thromboresistance, as well as excellent wear resistance.[8] In the present study, we used the Medtronic Hall valve, which has excellent durability and exceptionally low thrombogenicity.[9,10] The Medtronic Hall valve utilizes a disk consisting of a carbon substrate coated with pyrolytic carbon that pivots within a titanium housing; titanium is able to withstand considerable compressive stress. The flow through the major orifice of the tilting disc valve acts on the blood pump at the diaphragm–housing junction;[11] this creates a washout effect inside the blood pump that helps to prevent thrombosis. For this reason we selected the Medtronic Hall valve for use in our electrohydraulic total artificial heart (EHTAH). In our previous studies, mechanical heart valves (MHVs) were mounted on a rigid mounting by inserting the valve stopper in an EHTAH made of polyurethane after the MHV sewing ring had been removed; stronger cavitation intensity around the valve stop was then observed in in vitro testing.[12–14] The cavitation bubbles were concentrated at the valve stop; the major cause of this concentration was determined to be squeeze flow. The squeeze flow velocity was proportional to the valve-closing velocity just before valve closure.[13] The occurrence of strong cavitation could be estimated in in vivo testing. It is essential that the occurrence of cavitation be estimated by in vivo testing to prevent cavitation pitting of the valve surface and resultant blood damage.

The aim of this study was to observe MHV cavitation pits formed during in vivo testing of an EHTAH. In previous studies, we investigated the relationship between the

Received: August 18, 2008 / Accepted: April 4, 2009

H.S. Lee (✉) · A. Homma · E. Tatsumi · Y. Taenaka
Department of Artificial Organs, Research Institute, National Cardiovascular Center, 5-7-1 Fujishiro-dai, Suita, Osaka 565-8565, Japan
Tel. +81-6-6833-5004 ext. 2368; Fax +81-6-6835-5406
e-mail: hslee@ri.ncvc.go.jp

left driving pressure (LDP) and right driving pressure (RDP) slopes and cavitation intensity in in vitro testing. In in vivo testing with three sets of valves (one set used in two animals), the LDP was used as a factor for cavitation occurrence, and the occurrence of cavitation was determined by the observation of cavitation pits on the explanted valve surfaces.

Materials and methods

The EHTAH consists of two diaphragm-type blood pumps, an actuator, and a controller (Fig. 1). The actuator is connected to both blood pumps, which are filled with silicon oil. The silicon oil drives the blood pump by the forward and/or reverse rotation of the impeller inside the actuator. The rotational speed of the impeller and the systolic ratio are controlled by the controller. The total volume of the left and right blood pumps was 390 ml, and they had a stroke volume of 75 ml.[15] The valves mounted at the inlet and outlet ports of the blood pumps, respectively, were 25-mm and 23-mm Medtronic Hall valves (Medtronic, Minneapolis, MN, USA) (Fig. 1).

In vivo estimation of MHV cavitation in the EHTAH was performed using calves weighing 69–80 kg. The EHTAH was orthotopically placed in the pericardial space, and the internal battery and internal controller were implanted in subcutaneous pockets. The filling and ejection conditions of the left blood pump were monitored by the LDP and controlled by changing the heart rate and rotational speed. The adjusted pump rate ranged from 80 to 130 bpm and the left systolic ratio ranged from 45% to 60%. The motor rotational speed ranged from 1030 to 1480 rpm for the left systole and from 950 to 1390 rpm for the right systole (Table 1). The mean aortic pressure ranged from 80 to 130 mmHg and the mean left atrial pressure ranged from 0 to 30 mmHg.

Cardiac output was estimated using the full-filling and partial-filling signals of the LDP waves[12] and ranged from 4.0 to 6.2 l/min. The cavitation pits on the valve surface were examined by scanning electron micrography (SEM; VE-8800; Keyence, Osaka, Japan). As a clinical measurement of blood damage, we measured the degree of hemolysis using a biochemical analysis system (VetScan; Abaxis, Sunnyvale, CA, USA).

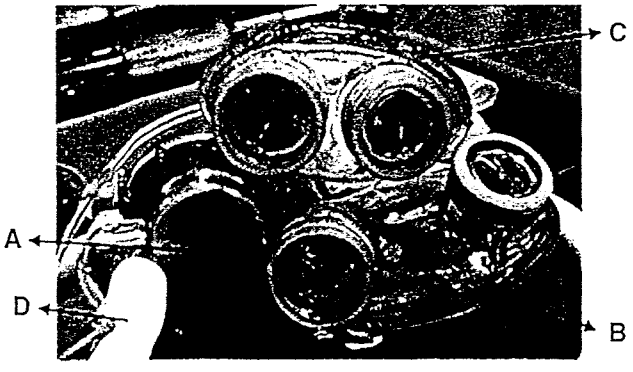

Fig. 1. The electrohydraulic total artificial heart (EHTAH). *A*, actuator; *B*, right blood pump; *C*, left blood pump; *D*, control cable

Results

An example of the LDP and RDP is shown in Fig. 2. The maximum and minimum LDPs ranged from 180 to 200 mmHg and from −20 to −80 mmHg, respectively, and

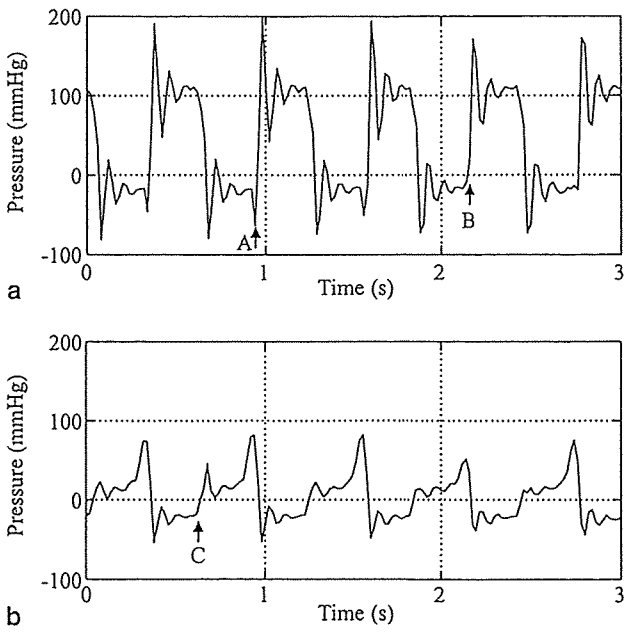

Fig. 2. Example of waves of left driving pressure (LDP) (a) and right driving pressure (RDP) (b) at a heart rate of 100 bpm. The *arrows* indicates the valve closure point: *A*, full filling; *B* partial filling; *C*, partial filling (full filling did not occur in the right side pump)

Table 1. Electrohydraulic total artificial heart running conditions for in vivo testing for the three sets of valves used in four calves

Valve	Survival time (days)	Weight (kg)	Heart rate (bpm)	Motor revolution speed for the left systole (rpm)	Motor revolution speed for the right systole (rpm)	Left systolic duration (%)	Cause of death
1	21	78	90–120	1250–1480	950–1190	47–50	Infection
2	[a]56(30)	70	90–120	1150–1360	850–1280	45–55	Respiratory failure
	(26)	80	80–120	1030–1380	1100–1210	48–61	System failure
3	70	69	100–130	1200–1390	1010–1390	51–60	Infection

[a]These valves were reused in a second animal experiment

the maximum and minimum RDPs ranged from 80 to 110 mmHg and from −10 to −60 mmHg. In our previous study, we confirmed that the LDP waves increased suddenly after valve closure in in vitro testing.[12] Using the same method as that used for in vitro testing, we were able to estimate the inlet valve closure point in the present study (arrows in Fig. 2). The EHTAH (Fig. 1) was run by silicon oil that drove the blood pump via inverse and/or reverse rotation of the impeller. The left and right blood pumps were alternately filled and ejected by displacement of the diaphragms. In the full-filling condition for the left blood pump (point A on Fig. 2a), the diaphragm of the left blood pump was pulled by the silicon oil force, and hence the LDP generated a negative pulse pressure. In the partial-filling condition (point B on Fig. 2a), the diaphragm was not pulled completely, and hence the negative peak pulse pressure of the LDP did not occur. The motor rotational speed for the right systole of the right blood pump was less than that of the left blood pump, resulting in the partial-filling condition only (point C on Fig. 2b). Even with the blood pump operating under stable conditions, the LDP slope 5 ms before valve closure was irregular, ranging from 6000 to 12000 mmHg/s. In contrast, the RDP slope 5 ms before valve closure ranged only from 3200 to 6300 mmHg/s.

An SEM image of a new valve surface is shown in Fig. 3: no surface pits were observed. In contrast, SEM photographs of the inlet valve surface of the right and left blood pumps for the three sets of valves used in in vivo testing are shown in Figs. 4–6. Cavitation pits were found to be concentrated around the valve stop. With respect to the inlet valve of the left blood pump, large cavitation pits reaching a maximum diameter of 1 μm were observed on the valve surface (Fig. 7).

As an index of blood damage, we measured the degree of hemolysis, and this remained at zero during all experiments, i.e., the plasma free hemoglobin level was below 20 mg/dl. In the present study, the causes of death were respiratory failure, system failure, and infection (see Table 1).

Discussion

In a previous study, we confirmed the presence of cavitation bubbles during in vitro testing, and we found that most of the cavitation bubbles were observed near the valve stop (Fig. 8).[12] This implied that the major cause of MHV cavitation was squeeze flow between the leaflet and the valve stop. MHV cavitation depended on the flow viscosity, the area of the valve stop, and the valve closing velocity. We used a glycerin solution with the same viscosity as blood in vitro as the test fluid. Therefore, our in vitro results might be useful in estimating the cavitation intensity in in vivo experiments. Moreover, we investigated the relationship between the LDP slope just before valve closure and cavitation intensity.[12] The cavitation visualization time is equal to the number of frames in which cavitation is observed divided by the frame rate of the high-speed camera. As shown in Fig. 9, we were able to estimate the maximum

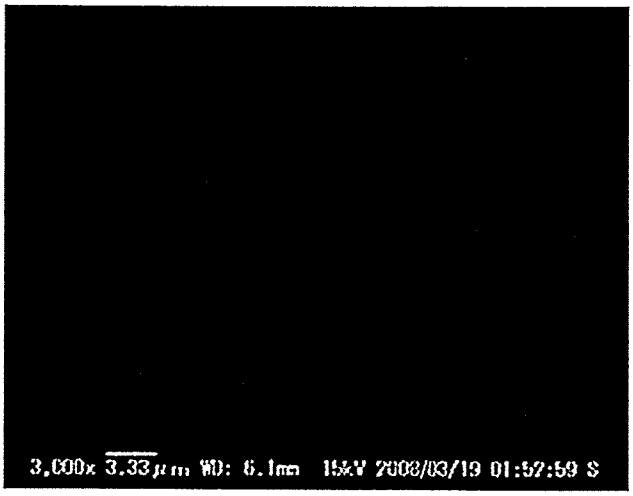

Fig. 3. Scanning electron micrograph of the new valve surface

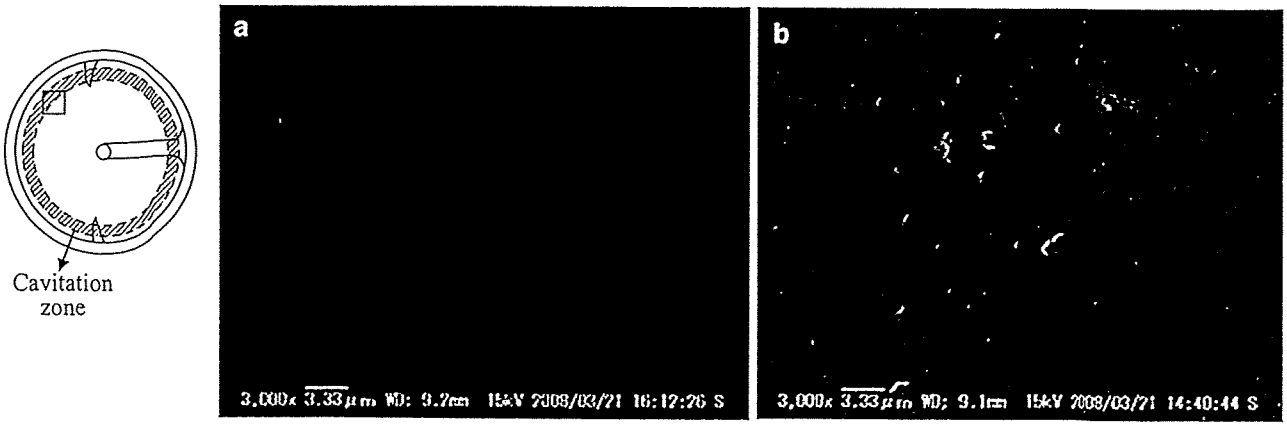

Fig. 4a,b. Scanning electron micrograph of the valve surfaces after the EHTAH had been implanted in a calf for 21 days. a Inlet valve surface of the right blood pump, b inlet valve surface of the left blood pump. The area shown is around the valve stop

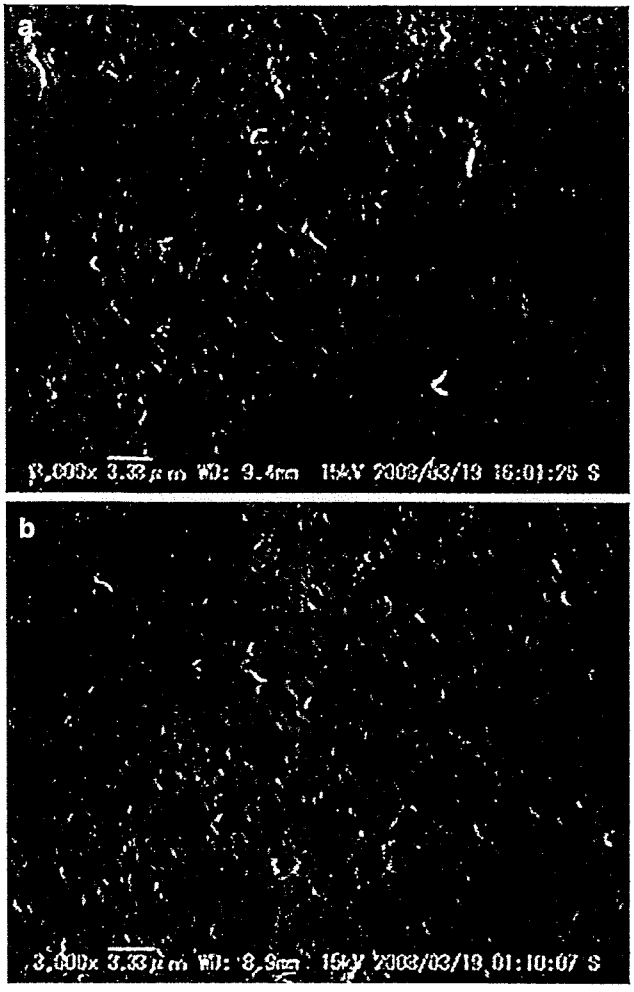

Fig. 5a,b. Scanning electron micrograph of the valve surfaces after 56 days of implantation in two calves. a Inlet valve surface of the right blood pump, b inlet valve surface of the left blood pump. These valves were used in two animal experiments

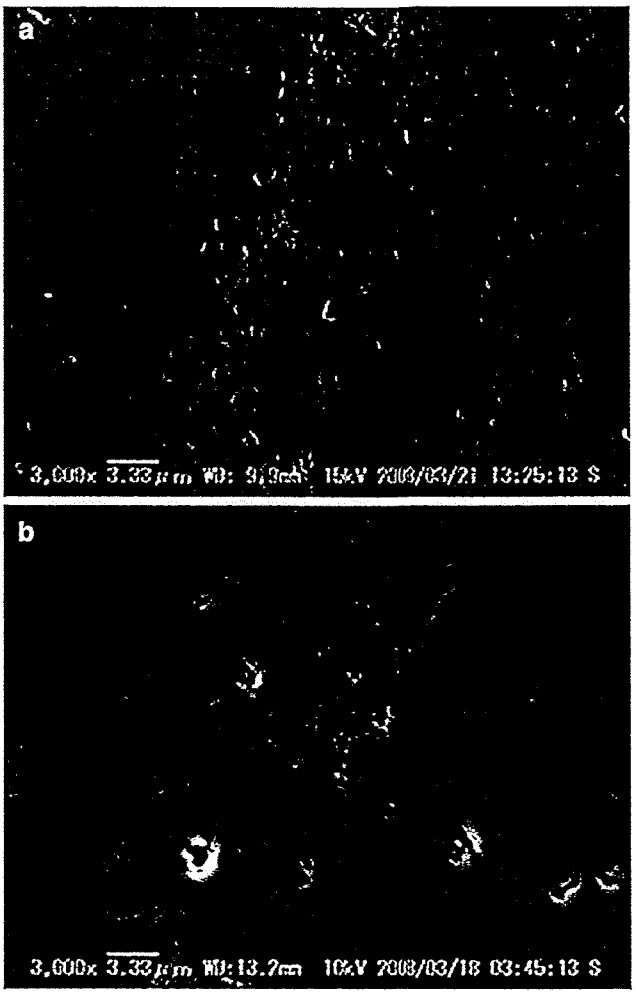

Fig. 6a,b. Scanning electron micrograph of the valve surface after 70 days of implantation in a calf. a Inlet valve surface of the right blood pump, b inlet valve surface of the left blood pump

valve-closing velocity as 3.8 m/s, while the maximum cavitation visualization time reached approximately 430 μs in in vivo testing. The cavitation visualization time can be calculated by Rayleigh analysis when a spherical cavity is present in an inviscid incompressible liquid:[2]

$$t_{visualization\ time} = 0.915 R_{max} \sqrt{\frac{\rho}{p_\infty}} \quad (1)$$

where ρ is the density of the liquid, R_{max} is the maximum radius of the cavitation bubble, and P_∞ is the pressure at infinity. From Eq. 1, we estimated a maximum diameter of approximately 2 mm in the present study. As shown in Eq. 1, the cavitation visualization time depends on the size of the cavitation bubbles. The peak pressure when a collapse of cavitation bubbles occurs is given roughly as:

$$P_{max} \approx 100 R_{max} \frac{P_\infty}{r}. \quad (2)$$

where r is the distance from the bubble center. Eq. 2 gives the order of magnitude of the strong pressure, which might

Fig. 7. Enlarged photograph of cavitation pits showing the valve surface after 56 days of implantation. The *circled area* shows overlapping pits

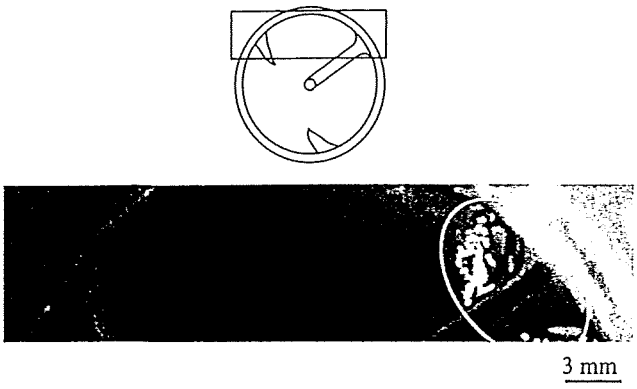

Fig. 8. Cavitation bubbles with a heart rate of 100 bpm in in vitro testing. Most of the cavitation bubbles were observed near the valve stop (from Lee et al.[12])

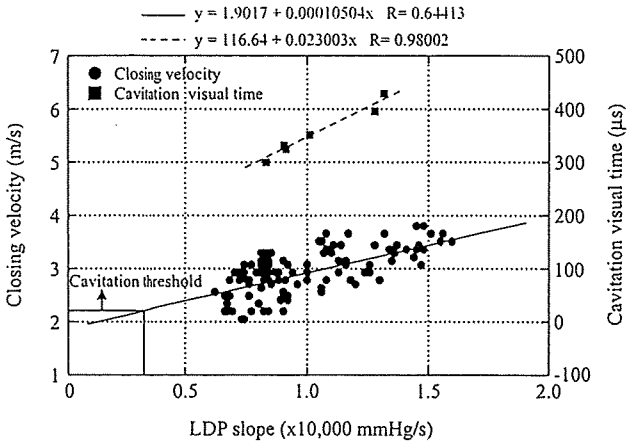

Fig. 9. Valve-closing velocity and cavitation visualization time at various LDP slopes in in vitro testing. The valve-closing velocity and the slope of the LDP were measured during the 5-ms interval immediately before valve closure. The cavitation visualization time is equal to the number of frames during which cavitation bubbles were visible multiplied by the interval of the frames (from Lee et al.[12])

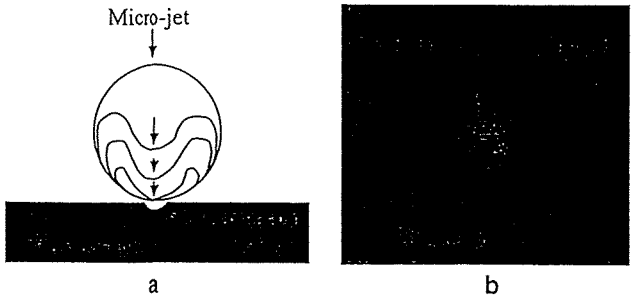

Fig. 10a,b. Mechanism of cavitation pitting on the valve surface. a Collapse of cavitation bubble causes a microjet, b configuration of a large cavitation pit on the valve surface

impinge on a solid surface a few radii away. For example, if $P_\infty \approx 0.1$ MPa this implies a substantial pulse of 10 MPa at a distance of one maximum bubble radius away. As shown in Eq. 2, the pressure due to cavitation bubble collapse increases as the bubble size increases. Furthermore, the high pressure caused by the collapse of the cavitation bubbles reaches 1 GPa at the bubble center.[1] Pyrolytic carbon is modestly tough, with flexural strength ranging from 350 to 530 MPa.[6] The high pressure caused by the collapsing cavitation bubbles generates a microjet and shock waves that exceed the flexural strength of pyrolytic carbon. An enlarged photograph of these cavitation pits is shown in Fig. 7. Cavitation pits are spherical, and the diameter of the overlapping pits in the present study exceeded 1 μm (Fig. 7).

In the present study, the cavitation pits on the valve surface were concentrated around the valve stop (Figs. 4–6), which is consistent with the cavitation bubble zone identified in in vitro testing.[12] Cavitation pits generated by cavitation bubbles cause squeeze flow between the leaflet and the valve stop. As shown in Figs. 4–6, large cavitation pits were observed at the inlet valve of the left blood pump. The LDP slope was higher than the RDP slope, and stronger and larger cavitation bubbles were generated in the inlet of the left blood pump than in that of the right blood pump. When large cavitation bubbles near the valve surface collapsed (Fig. 10a), a high-speed microjet originated from the bubble center.[1] This suggests overlapping multiple pitting (Fig. 10b), which raises the possibility that deeper and wider cavitation pits might form with long-term exposure to cavitation (circle in Fig. 7). In a previous study, cavitation pits of a model disc valve were examined using a simple solenoid-actuated apparatus that could directly control the closing velocity of a model disc valve. It was demonstrated that the number of pits and their size is proportional to the closing velocity and the number of opening and closing cycles.[16] In the present study, even though we used a different valve, longer implantation times tended to cause increased numbers of cavitation pits with larger sizes, which agreed with previous results. The cavitation pits on the valve surface in in vivo testing will eventually lead to leaflet fracture. High driving pressure slopes lead to an increase in both the number of cavitation pits and the area in which cavitation pits occur. The present EHTAH does not have a compliant structure and the experimental operating conditions were more severe than those of the natural heart. Therefore, even with the relatively small number of 2.7 – 13.1 $\times 10^6$ cycles (equal to 21–70 days of operation), cavitation pits were observed on the valve surface. This indicates that the durability of the MHV is an important factor if it is used in an artificial heart.

Several articles have indicated that full-filling and full-ejection conditions decrease cavitation,[6,17,18] which were contradictory findings to our results. We believe that these differences may result from differences in the driving system for the blood pump and the pump size. Lukic et al. used a pediatric pulsatile VAD with a stroke volume of 15 ml,[17] and Zapanta et al. used an electrical VAD of the pusher-plate type.[6] Our EHTAH is of the diaphragm type, so the ventricular pressure suddenly increases during the systolic phase. In a previous study, we confirmed that the slope of the ventricular pressure and the valve-closing velocity during full-filling and full-ejection conditions were higher than those for partial filling and partial ejection.[12] Our

results of the relationship between the driving condition for the blood pump and the cavitation intensity differ to other groups' results; however, the cavitation intensity depended on the valve-closing velocity both in our group and in other groups. In this study, we consider that the partial-filling and partial-ejection condition is desirable to prevent hemolysis and heart valve damage.

In this study, in order to estimate the blood damage, we measured the degree of hemolysis using a biochemical analysis system during the experiment. The degree of hemolysis remained at zero, which means that the plasma free hemoglobin was below 20 mg/dl. This means that there was no significant hemolysis in our EHTAH. Even if cavitation pits were observed on the valve surfaces, we did not observe significant blood damage. In a previous study, we found that the area in which cavitation bubbles occurred was small, which caused a small amount of blood damage.

In this study, we investigated the cavitation pits created when using a tilting disc valve in our EHTAH; however, tilting disc valves are no longer commonly used clinically, and they will be difficult to obtain in the future. Moreover, the majority of MHVs currently in clinical use are bileaflet valves, which have low pressure gradients, central flow, and large effective orifice areas, and have proven to have superior hydrodynamic characteristics to those of tilting disc valves. Therefore, in the future, we will attempt to investigate flow visualization inside the blood pump using a bileaflet valve in our artificial heart.

Conclusions

In the present study, we investigated cavitation pits formed on the inlet valve surfaces of both the left and right blood pump of an EHTAH during in vivo testing. The presence of cavitation was determined by observation of cavitation pits on the explanted valve surfaces in three sets of valves used in four animals. The longer the time of pump operation, the larger the cavitation pit number and size tended to be. A high driving pressure slope was found to correspond to an increase in the size of the area in which cavitation pits were observed. Thus, when estimating cavitation intensity in in vivo testing, both a high driving pressure slope and operational time are important factors. The cavitation pits observed on valve surfaces in in vivo testing will eventually lead to leaflet fracture.

References

1. Knapp RT, Daily JW, Hammitt FG. Cavitation. Iowa: Institute of Hydraulic Research, University of Iowa, 1979;218–223
2. Brennen CE. Cavitation and bubble dynamics. New York: Oxford University Press, 1995
3. Klepetko W, Moritz A, Mlczoch J, Schurawitzki H, Domanig E, Wolner E. Leaflet fracture in Edward-Duromedics bileaflet valves. J Thorac Cardiovasc Surg 1989;97:90–94
4. Kafesjian R, Howanec M, Ward GD, Diep L, Wagstaff LS, Rhee R. Cavitation damage of pyrolytic carbon in mechanical heart valves. J Heart Valve Dis 1994;3(Suppl. 1):S2–S7
5. Bottio T, Casarotto D, Thiene G, Caprili L, Angelini A, Gerosa G. Leaflet escape in a new bileaflet mechanical valve: TRI technologies. Circulation 2003;107:2303–2306
6. Zapanta CM, Stinebring DR, Sneckenberger DS, Deutsch S, Geselowitz DB, Tarbell JM, Snyder AJ, Rosenberg SG, Weiss WW, Pae WE, Pierce W. In vivo observation of cavitation on prosthetic heart valves. ASAIO J 1996;42:M550–M555
7. Graf T, Fischer H, Reul H, Rau G. Cavitation potential of mechanical heart valve prostheses. Int J Artif Organs 1991;14:169–174
8. Ryder JK, Cao H. Structural integrity assessment of heart valve prostheses: a damage tolerance analysis of the CarboMedics prosthetic heart valve. J Heart Valve Dis 1996;5(Suppl. 1):S86–S96
9. Akins CW. Review of the global experience with the Medtronic Hall valve. Eur J Cardiothorac Surg 1992;6(Suppl. 1):S68–S74
10. Butchart EG, Li HH, Payne N, Buchan K, Grunkemerier GL. Twenty years' experience with the Medtronic Hall valve. J Thorac Cardiovasc Surg 2001;121:1090–1100
11. Nakata M, Masuzawa T, Tatsumi E, Taenaka Y, Nishimura T, Tsukiya T, Takano H, Tsuchimoto K, Ohba K. Characterization and optimization of the flow pattern inside a diaphragm blood pump based on flow visualization techniques. ASAIO J 1998;44: M714–M718
12. Lee HS, Taenaka Y, Kitamura S. Estimation of mechanical heart valve cavitation in an electro-hydraulic total artificial heart. Artif Organs 2006;30:16–23
13. Lee HS, Taenaka Y, Kitamura S. Mechanism for cavitation in the mechanical heart valve with an artificial heart: nuclei and viscosity dependence. Artif Organs 2005;29:41–46
14. Lee HS, Taenaka Y, Kitamura S. Cavitation phenomenon in monoleaflet mechanical heart valve with electrohydraulic total artificial heart. Int J Artif Organs 2004;27:779–786
15. Tatsumi E, Taenaka Y, Uesho K, Homma A, Nishinaka T, Kakuta Y, Tsukiya T, Takano H, Masuzawa T, Nakamura M, Koshiji K, Fukui Y, Tsukahara K, Tsuchimoto K, Wakui H. Current status of development and in vivo evaluation of the National Cardiovascular Center electrohydraulic total artificial heart system. J Artif Organs 2000;3:62–69
16. Lee HS, Yamamoto K, Kudo N, Shimooka T, Mitamura Y, Yuhta T. Examination of cavitation-induced surface erosion pitting of a mechanical heart valve using closing velocity. J Artif Organs 2002;5:193–199
17. Lukic B, Zapanta CM, Griffith KA, Weiss WJ. Effect of the diastolic and systolic duration on valve cavitation in a pediatric pulsatile ventricular assist device. ASAIO J 2005;51:546–550
18. Garrison LA, Lamson TC, Deutsch S, Geselowitz DB, Gaumond RP, Tarbell JM. An in-vitro investigation of prosthetic heart valve cavitation in blood. J Heart Valve Dis 1994;3 (Suppl. 1):S8–S24

J Artif Organs (2009) 12:98–104
DOI 10.1007/s10047-009-0453-8

ORIGINAL ARTICLE

Hwansung Lee, PhD · Yoshiaki Ikeuchi, MS
Eiki Akagawa, PhD · Eisuke Tatsumi, PhD
Yoshiyuki Taenaka, PhD · Takao Yamamoto, PhD

Effects of leaflet geometry on the flow field in three bileaflet valves when installed in a pneumatic ventricular assist device

Abstract Our group is currently developing a pneumatic ventricular assist device (PVAD). In this study, in order to select the optimal bileaflet valve for our PVAD, three kinds of bileaflet valve were installed and the flow was visualized downstream of the outlet valve using the particle image velocimetry (PIV) method. To carry out flow visualization inside the blood pump and near the valve, we designed a model pump that had the same configuration as our PVAD. The three bileaflet valves tested were a 21-mm ATS valve, a 21-mm St. Jude valve, and a 21-mm Sorin Bicarbon valve. The mechanical heart valves were mounted at the aortic position of the model pump and the flow was visualized by using the PIV method. The maximum flow velocity was measured at three distances (0, 10, and 30 mm) from the valve plane. The maximum flow velocity of the Sorin Bicarbon valve was less than that of the other two valves; however, it decreased slightly with increasing distance it the X-Y plane in all three valves. Although different bileaflet valves are very similar in design, the geometry of the leaflet is an important factor when selecting a mechanical heart valve for use in an artificial heart.

Key words Pneumatic ventricular assist device · Bileaflet mechanical heart valve · Flow visualization · Particle image velocimetry

Introduction

The use of a mechanical circulatory support device such as an artificial heart or a ventricular assist device (VAD) has become standard therapy as a bridge to transplantation. In recent years, the most frequently used devices are the pulsatile VAD, e.g., the Berlin Heart VAD, the Thoratec VAD, the Novacor II, the WorldHeart HeartSaver VAD, and the Arrow LionHeart VAD.[1] The Berlin Heart VAD uses a tilting disc and a polyurethane velum valve, the Thoratec VAD and the Arrow LionHeart VAD each use a tilting disc valve, the Novacor II uses a bovine pericardial tissue valve, and the WorldHeart HeartSaver VAD uses a tilting disc and a tissue valve. The flow through the major orifice of the tilting disc valve acts on the blood pump in the diaphragm–housing junction,[2] creating a washout effect inside the blood pump that helps to prevent thrombosis. For this reason, we had previously developed a pulsatile pneumatic ventricular assist device (PVAD) that employed a tilting disc valve. Now, however, tilting disc valves are no longer commonly used clinically, and they will be difficult to obtain in the future. The majority of mechanical heart valves (MHVs) currently in clinical use are bileaflet valves, which have low pressure gradients, central flow, and large effective orifice areas, and have proven to have superior hydrodynamic characteristics to those of tilting disc valves. Therefore, we are attempting to use a bileaflet valve in our PVAD.

Cavitation and high shear stress are major causes of blood cell trauma,[3–5] and cavitation has also been widely studied as one of the causes of MHV damage.[6–11] When the valve closes and local pressure falls below the vapor pressure of the liquid, cavitation bubbles form. When these bubbles collapse, high pressure is generated by the resultant shock waves and microjets. When the valve then opens, high-speed flow is generated, causing blood cell trauma. Many research groups have visualized the flow of MHVs under various physiological conditions.[12–17] However, an artificial heart must sometimes operate under severe conditions, and its flow velocity pattern may therefore differ from the patterns that occur under ordinary physiological conditions.

In our previous studies, we investigated cavitation intensity with the MHV at the mitral position.[18,19] We found that even higher stress was generated at the aortic position, which also causes blood cell trauma. In the present study, in order to select the optimal bileaflet valve for our PVAD,

Received: April 10, 2008 / Accepted: March 1, 2009

H.S. Lee (✉) · E. Akagawa · E. Tatsumi · Y. Taenaka
Department of Artificial Organs, Research Institute, National Cardiovascular Center, 5-7-1 Fujishiro-dai, Suita, Osaka 565-8565, Japan
Tel. +81-6-6833-5004 ext. 2368; Fax +81-6-6835-5406
e-mail: hslee@ri.ncvc.go.jp

Y. Ikeuchi · T. Yamamoto
Graduate School of Engineering, Osaka University, Osaka, Japan

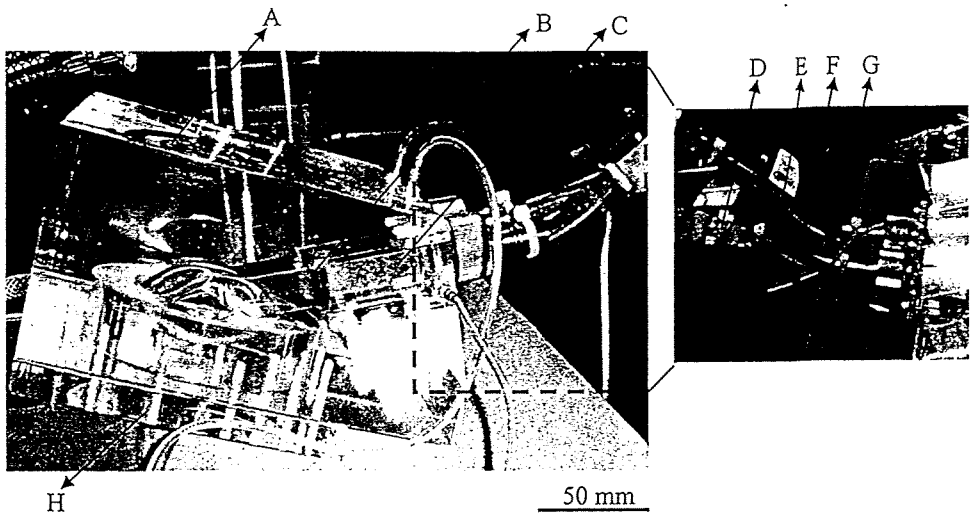

Fig. 1. Configuration of the model pump. The model pump was made of acrylic resin to allow optical access to the flow velocity of the blood pump. *A*, model pump; *B*, valve mount; *C*, valve mounting pipe; *D*, inlet port of the polystyrene tracer; *E*, ultrasound flow meter; *F*, inlet port; *G*, outlet port; *H*, back plate

three different valves were installed, and we visualized the flow downstream of the outlet valve using the particle image velocimetry (PIV) method.

Materials and methods

Model pump

To visualize the flow inside the blood pump and downstream of the MHV in our new PVAD,[20] a model pump unit consisting of a model pump, a back plate, and a valve mounting pipe was constructed of acrylic resin to allow optical access to the internal flow field (Fig. 1). The MHV was installed in the valve mount and fixed to the model pump using valve mounting pipes made of acrylic resin (Fig. 1). To allow the fluid to sink easily, there is a 1-mm gap between the model pump and the valve mounting pipes. The model pump was connected to a Donovan mock circulatory loop tester. The mean aortic and left atrial pressures were maintained at 100 and 7 mmHg, respectively, and were measured by a pressure transducer (MP5100; Baxter, Deerfield, IL, USA) with a sampling frequency of 1 kHz. The model pump was operated at a positive pressure of 250 mmHg and a negative pressure of −60 mmHg, relative to atmospheric pressure, with a control–drive console for circulatory support (VCT-30; Toyobo, Osaka, Japan). The model pump ran at a heart rate of 70 beats/min and a systolic duration of 31%, which results in a bypass flow of 4.5 l/min. As working fluid, a combination of 64% sodium iodide and 36% distilled water by weight was used. This blood analog fluid has a viscosity of 3.3 cP, a density of 1.9 g/cm^3 at 20°C, and a refractive index of 1.49, which is close to that of the acrylic resin. Bypass flow was measured using an ultrasound flow meter (T106; Transonic Systems, Ithaca, NY, USA) placed at the outflow side of the model pump (Fig. 1).

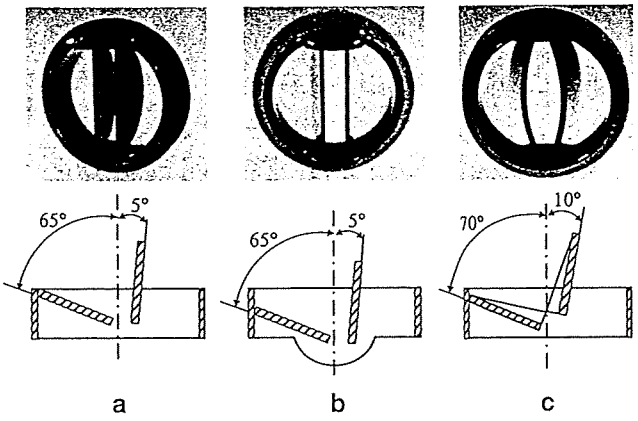

Fig. 2. The bileaflet valves used in this study: a ATS valve, b St. Jude valve, c Sorin Bicarbon valve

Valve testing

A 21-mm ATS valve (ATS Medical, Minneapolis, MN, USA), a 21-mm St. Jude valve (St. Jude Medical, St. Paul, MN, USA), and a 21-mm Sorin Bicarbon valve (Sorin Biomedica, Vercelli, Italy) were each mounted on the model pump after removing the sewing ring (Fig. 2). The configuration of the bileaflet valves is shown in Table 1. Although the sewing ring diameter was identical in the three different bileaflet valves, they had different orifice diameters and outer ring diameters once the sewing ring was removed. In order to remove the effect of the inlet valve on the flow pattern inside the model pump, a 21-mm Medtronic Hall valve (Medtronic, Minneapolis, MN, USA) was installed on the outlet port. For the inlet valve, the major orifice direction of the monoleaflet valve was set at a 180° clockwise orientation (Fig. 3). For the outlet valve, the leaflet tip direction of the bileaflet valves were set at 90° and 180°, respectively.

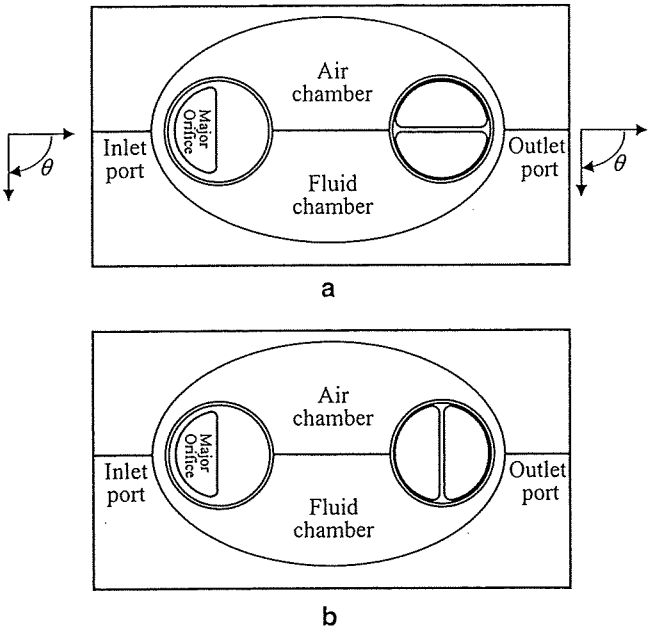

Fig. 3. Valve orientation angle for the inlet and outlet ports: **a** X-Y plane, **b** X-Z plane

Table 1. Configuration of the bileaflet valves

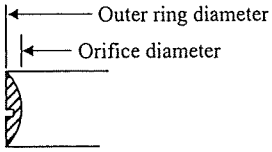

Valves	Sewing ring diameter	Outer ring diameter	Orifice diameter	Opening angle
ATS valve	21 mm	18.2 mm	14.8 mm	85 degree
St. Jude valve	21 mm	18.4 mm	14.7 mm	85 degree
Sorin valve	21 mm	18.7 mm	15.2 mm	80 degree

PIV method

A polystyrene tracer with a diameter of 50 μm and a density of 1.06 g/cm^2 (Vestosint; Degussa, Düsseldorf, Germany) was added to the fluid and visualized on a laser sheet by two argon-ion laser probes with a 488-nm wavelength (GLG3680: 333–529 nm, maximum power 15W; NEC, Tokyo, Japan) (Fig. 4). The laser beam took the form of a planar sheet approximately 1 mm thick and was shed across the center of the valve. The laser light was reflected by the polystyrene tracer dispersed in the blood analog fluid at room temperature, and the captured tracer images were recorded at 3000 frames/s with a high-speed camera (Memrecam fx-6000; NAC Image Technology, Tokyo, Japan) for 4 s. The laser sheet illuminated two different planes: the X-Y plane and the X-Z plane. The flow velocity vectors were measured using PIV software (Insight 3.0; TSI, Shoreview, MN, USA) and the vector files were loaded into the Tecplot program (version 9.2; Tecplot, Bellevue, WA, USA) to present the PIV data graphically. Phase averaging was performed over

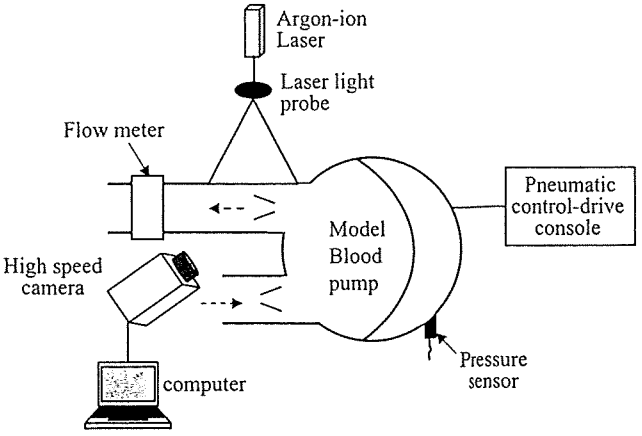

Fig. 4. Diagram of the experimental system. Images of the flow were recorded continuously at 3000 frames/s with a high-speed camera. The flow velocity was calculated from the images obtained

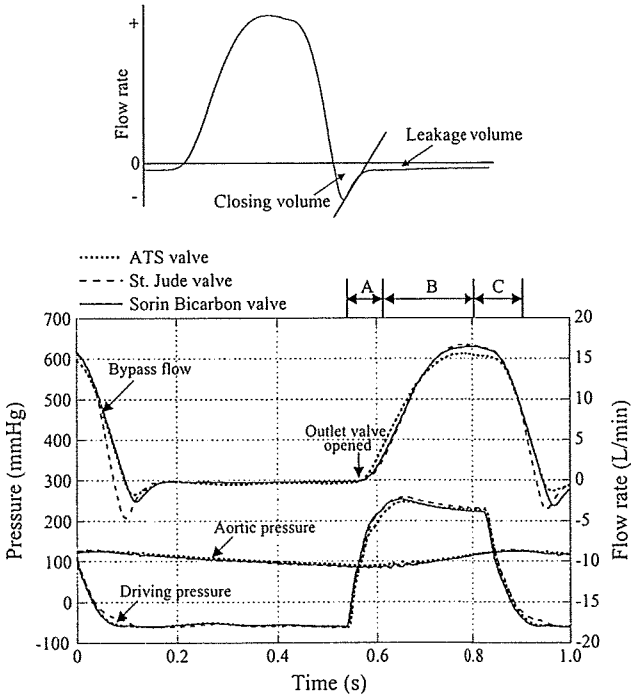

Fig. 5. Driving pressure, aortic pressure, and bypass flow waves. The driving pressure was used to trigger signals. The zero time was the trigger point. *A*, early systole region; *B*, mid-systole region; *C*, end systole region

three cycles. Because the polystyrene tracer has a lower density than that of the working fluid, it floats when added to the working fluid. Therefore, we installed an inlet port at the front of the inlet valve (Fig. 1) and then put the polystyrene tracer into the model pump using a syringe just before recording the PIV images from that port.

Results

The driving pressure and bypass flow waves are shown in Fig. 5. The bypass flow waves were measured at the outflow

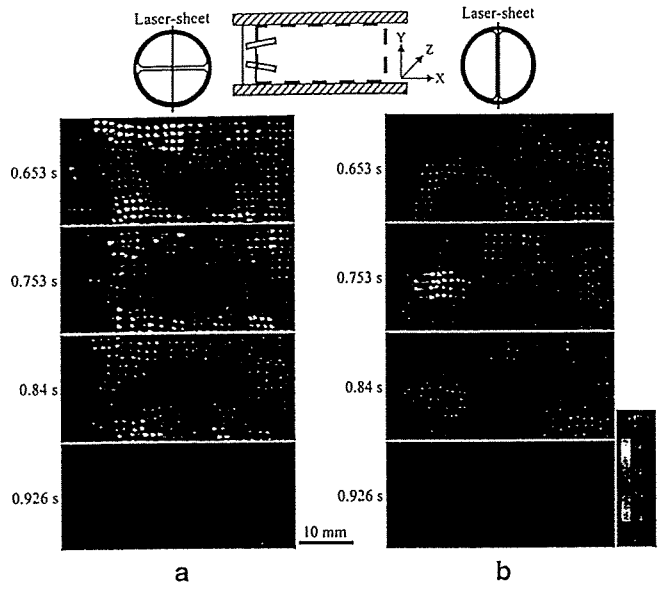

Fig. 6. Particle image velocimetry (PIV) flow velocity vectors for the ATS valve: a X-Y plane, b X-Z plane. The timing means the time elapsed from the trigger point

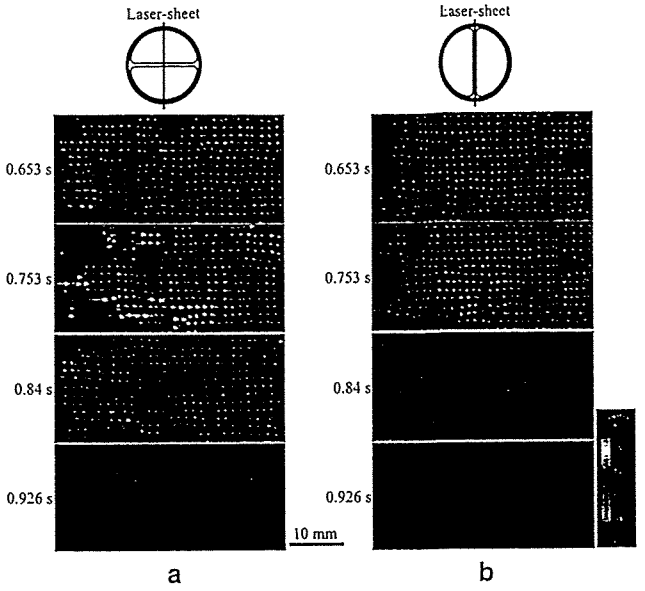

Fig. 7. PIV flow velocity vectors for the St. Jude valve: a X-Y plane, b X-Z plane. The time is the same as in Fig. 5. The timing means the time elapsed from the trigger point

side of the model pump. From the bypass flow waves, we were able to estimate the point at which the outlet valve opened, i.e., when the driving pressure was above the aortic pressure (Fig. 5). The valve opening point did not differ among the three kinds of bileaflet valve. However, as shown in Fig. 5, the bypass flow was slightly different among the three kinds of bileaflet valves. During the early systolic period, the bypass flow of the ATS valve was greater than that of the other valves. On the other hand, the closing volume of the St. Jude valve was larger than that of the other valves.

The flow velocity vectors downstream of the bileaflet valves during the systolic phase of the cardiac cycle are shown in Figs. 6–8. In the case of the ATS valve, higher flow velocities were observed at the upper and lower sides of the X-Y plane during the mid-systole phase. Higher flow velocities were also observed at the central line of the X-Z plane during the mid-systole phase. The flow velocity in the X-Y plane was higher than that in the X-Z plane (Fig. 6). In the case of the St. Jude valve, the highest jet flow occurred in the X-Y plane near the leaflet (Fig. 7a); no higher flow velocity was observed in the X-Z plane (Fig. 7b). In the case of the Sorin Bicarbon valve, there was no fast flow velocity region (Fig. 8). In all bileaflet valves, the flow velocity in the X-Y plane was higher than that in the X-Z plane (Figs. 6–8). In case of the ATS valve, turbulent flow was observed during the mid-systole phase in the X-Y plane (center line at a time of 0.753 s in Fig. 6a). Moreover, the possibility of turbulent flow was also observed near the leaflet during the mid-systole phase in the X-Z plane (at a time of 0.753 s in Fig. 6b). Regurgitation was observed during the early diastole phase (at a time of 0.926 s in Figs. 6–8).

One cycle of the maximum flow velocities at distances of 0, 10, and 30 mm from the valve plane were plotted (Figs. 9–11). The averaging of the maximum velocity was performed over three cycles. The average maximum flow

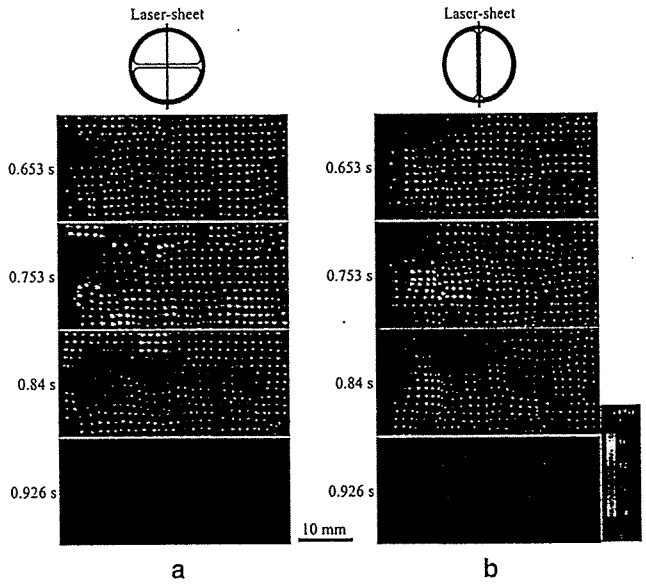

Fig. 8. PIV flow velocity vectors for the Sorin Bicarbon valve: a X-Y plane, b X-Z plane. The time is the same as in Fig. 5. The timing means the time elapsed from the trigger point

velocity of the ATS valve was greater than 2.0 m/s, ranging from 0.96 ± 0.12 to 2.46 ± 0.22 m/s, and decreased with increasing distance in the X-Y plane, with large fluctuations during the systole phase (Fig. 9a). The average maximum flow velocity in the X-Z plane ranged from 0.5 ± 0.07 to 1.47 ± 0.12 m/s and was less than that in the X-Y plane (Fig. 9b). The average maximum flow velocity of the St. Jude valve in the X-Y plane ranged from 1.02 ± 0.09 to 1.97 ± 0.11 m/s, with a large fluctuation during the systole phase (Fig. 10a). However, in the X-Z plane, the maximum flow velocity ranged from 0.95 ± 0.08 to 1.42 ± 0.11 m/s, and had small fluctuations (Fig. 10b). The maximum flow velocity of the Sorin Bicarbon valve ranged from 0.98 ± 0.11 to 1.5 ±